

Backward electroproduction of π^0 mesons on protons in the region of nucleon resonances at four momentum transfer squared $Q^2 = 1.0$ GeV 2

G. Laveissière,¹ N. Degrande,² S. Jaminion,¹ C. Jutier,^{1,3} L. Todor,³ R. Di Salvo,¹ L. Van Hoorebeke,² L.C. Alexa,⁴ B.D. Anderson,⁵ K.A. Aniol,⁶ K. Arundell,⁷ G. Audit,⁸ L. Auerbach,⁹ F.T. Baker,¹⁰ M. Baylac,⁸ J. Berthot,¹ P.Y. Bertin,¹ W. Bertozzi,¹¹ L. Bimbot,¹² W.U. Boeglin,¹³ E.J. Brash,⁴ V. Breton,¹ H. Breuer,¹⁴ E. Burtin,⁸ J.R. Calarco,¹⁵ L.S. Cardman,¹⁶ C. Cavata,⁸ C.-C. Chang,¹⁴ J.-P. Chen,¹⁶ E. Chudakov,¹⁶ E. Cisbani,¹⁷ D.S. Dale,¹⁸ C.W. de Jager,¹⁶ R. De Leo,¹⁹ A. Deur,^{1,16} N. d'Hose,⁸ G.E. Dodge,³ J.J. Domingo,¹⁶ L. Elouadrhiri,¹⁶ M.B. Epstein,⁶ L.A. Ewell,¹⁴ J.M. Finn,⁷ K.G. Fissum,¹¹ H. Fonvieille,¹ G. Fournier,⁸ B. Frois,⁸ S. Frullani,¹⁷ C. Furget,²⁰ H. Gao,¹¹ J. Gao,¹¹ F. Garibaldi,¹⁷ A. Gasparian,^{21,18} S. Gilad,¹¹ R. Gilman,^{22,16} A. Glamazdin,²³ C. Glashausser,²² J. Gomez,¹⁶ V. Gorbenko,²³ P. Grenier,¹ P.A.M. Guichon,⁸ J.O. Hansen,¹⁶ R. Holmes,²⁴ M. Holtrop,¹⁵ C. Howell,²⁵ G.M. Huber,⁴ C.E. Hyde-Wright,³ S. Incerti,⁹ M. Iodice,¹⁷ J. Jardillier,⁸ M.K. Jones,⁷ W. Kahl,²⁴ S. Kamalov,²⁶ S. Kato,²⁷ A.T. Katramatou,⁵ J.J. Kelly,¹⁴ S. Kerhoas,⁸ A. Ketikyan,²⁸ M. Khayat,⁵ K. Kino,²⁹ S. Kox,²⁰ L.H. Kramer,¹³ K.S. Kumar,³⁰ G. Kumbartzki,²² M. Kuss,¹⁶ A. Leone,³¹ J.J. LeRose,¹⁶ M. Liang,¹⁶ R.A. Lindgren,³² N. Liyanage,¹¹ G.J. Lulos,⁴ R.W. Lourie,³³ R. Madey,⁵ K. Maeda,²⁹ S. Malov,²² D.M. Manley,⁵ C. Marchand,⁸ D. Marchand,⁸ D.J. Margaziotis,⁶ P. Markowitz,¹³ J. Marroncle,⁸ J. Martino,⁸ C.J. Martoff,⁹ K. McCormick,³ J. McIntyre,²² S. Mehrabyan,²⁸ F. Merchez,²⁰ Z.E. Meziani,⁹ R. Michaels,¹⁶ G.W. Miller,³⁰ J.Y. Mougey,²⁰ S.K. Nanda,¹⁶ D. Neyret,⁸ E.A.J.M. Offermann,¹⁶ Z. Papandreou,⁴ C.F. Perdrisat,⁷ R. Perrino,³¹ G.G. Petratos,⁵ S. Platchkov,⁸ R. Pomatsalyuk,²³ D.L. Prout,⁵ V.A. Punjabi,³⁴ T. Pussieux,⁸ G. Quéménér,^{1,7} R.D. Ransome,²² O. Ravel,¹ J.S. Real,²⁰ F. Renard,⁸ Y. Roblin,¹ D. Rowntree,¹¹ G. Rutledge,⁷ P.M. Rutt,²² A. Saha,¹⁶ T. Saito,²⁹ A.J. Sarty,³⁵ A. Serdarevic,^{4,16} T. Smith,¹⁵ G. Smirnov,¹ K. Soldi,³⁶ P. Sorokin,²³ P.A. Souder,²⁴ R. Suleiman,¹¹ J.A. Templon,¹⁰ T. Terasawa,²⁹ L. Tiator,²⁶ R. Tieulent,²⁰ E. Tomasi-Gustafsson,⁸ H. Tsubota,²⁹ H. Ueno,²⁷ P.E. Ulmer,³ G.M. Urciuoli,¹⁷ R. Van De Vyver,² R.L.J. Van der Meer,^{16,4} P. Vernin,⁸ B. Vlahovic,^{16,36} H. Voskanyan,²⁸ E. Voutier,²⁰ J.W. Watson,⁵ L.B. Weinstein,³ K. Wijesooriya,⁷ R. Wilson,³⁷ B.B. Wojtsekhowski,¹⁶ D.G. Zainea,⁴ W-M. Zhang,⁵ J. Zhao,¹¹ and Z.-L. Zhou¹¹

(The Jefferson Lab Hall A Collaboration)

¹Université Blaise Pascal/IN2P3, F-63177 Aubière, France

²University of Gent, B-9000 Gent, Belgium

³Old Dominion University, Norfolk, VA 23529

⁴University of Regina, Regina, SK S4S OA2, Canada

⁵Kent State University, Kent OH 44242

⁶California State University, Los Angeles, CA 90032

⁷College of William and Mary, Williamsburg, VA 23187

⁸CEA Saclay, F-91191 Gif-sur-Yvette, France

⁹Temple University, Philadelphia, PA 19122

¹⁰University of Georgia, Athens, GA 30602

¹¹Massachusetts Institute of Technology, Cambridge, MA 02139

¹²Institut de Physique Nucléaire, F-91406 Orsay, France

¹³Florida International University, Miami, FL 33199

¹⁴University of Maryland, College Park, MD 20742

¹⁵University of New Hampshire, Durham, NH 03824

¹⁶Thomas Jefferson National Accelerator Facility, Newport News, VA 23606

¹⁷INFN, Sezione Sanità and Istituto Superiore di Sanità, 00161 Rome, Italy

¹⁸University of Kentucky, Lexington, KY 40506

¹⁹INFN, Sezione di Bari and University of Bari, 70126 Bari, Italy

²⁰Laboratoire de Physique Subatomique et de Cosmologie, F-38026 Grenoble, France

²¹Hampton University, Hampton, VA 23668

²²Rutgers, The State University of New Jersey, Piscataway, NJ 08855

²³Kharkov Institute of Physics and Technology, Kharkov 61108, Ukraine

²⁴Syracuse University, Syracuse, NY 13244

²⁵Duke University, Durham, NC 27706

²⁶Institut fuer Kernphysik, University of Mainz, D-55099 Mainz, Germany

²⁷Yamagata University, Yamagata 990, Japan

²⁸Yerevan Physics Institute, Yerevan 375036, Armenia

²⁹Tohoku University, Sendai 980, Japan

³⁰Princeton University, Princeton, NJ 08544

³¹INFN, Sezione di Lecce, 73100 Lecce, Italy

³²University of Virginia, Charlottesville, VA 22901

³³*State University of New York at Stony Brook, Stony Brook, NY 11794*³⁴*Norfolk State University, Norfolk, VA 23504*³⁵*Florida State University, Tallahassee, FL 32306*³⁶*North Carolina Central University, Durham, NC 27707*³⁷*Harvard University, Cambridge, MA 02138*

Exclusive electroproduction of π^0 mesons on protons in the backward hemisphere has been studied at $Q^2 = 1.0$ GeV 2 by detecting protons in the forward direction in coincidence with scattered electrons from the 4 GeV electron beam in Jefferson Lab's Hall A. The data span the range of the total ($\gamma^* p$) center-of-mass energy W from the pion production threshold to $W = 2.0$ GeV. The differential cross sections $\sigma_T + \epsilon \sigma_L$, σ_{TL} , and σ_{TT} were separated from the azimuthal distribution and are presented together with the MAID [1, 2, 3] and SAID [4, 5, 6] parametrizations.

PACS numbers: 23.23.+x, 56.65.Dy

I. INTRODUCTION

The present experiment [7] exploits the attractive opportunity to investigate a number of resonance states by detecting their decay into two channels of very similar kinematics, but remarkably different final-state interaction (FSI) couplings. They are:

$$e^- + p \rightarrow e^- + p + \pi^0 \quad (1)$$

and

$$e^- + p \rightarrow e^- + p + \gamma. \quad (2)$$

The intermediate resonant state decays via the strong interaction in reaction (1), and via the electromagnetic interaction in reaction (2). However, one can employ an identical technique for detecting two of the three outgoing particles for both reactions, namely detection of the scattered electron and proton in coincidence. This results in a greater precision for the relative cross sections of the two reactions than for either cross section alone.

A comparison of reactions (1) and (2) may be beneficial in addressing the problem of the "missing" resonances. The Constituent Quark Model (CQM) [8] predicts several positive parity states at $W > 1.6$ GeV that have not been observed [9, 10, 11, 12, 13]. It is conjectured that these states couple relatively weakly to the πN channel which has dominated (either in the initial or final state) most of the experimental work to date. The two reactions (1) and (2) provide therefore a potentially very different sensitivity to the missing resonances.

Closely related to reactions (1) and (2) is the process of deep inelastic electron scattering, which is generally analysed in terms of parton rather than baryon resonance degrees of freedom. However, the phenomenon of quark-hadron duality illustrates the interplay of these two frameworks at modest Q^2 and W [14, 15]. Another motivation for the present study is to explore the exclusive reactions (1) and (2) in the high energy limit, where current quark degrees of freedom may play as important a role as resonance, or constituent quark, degrees of freedom.

In the absence of a theoretical approach based on fundamental principles, one has to rely on experimental input and use phenomenological models. In the region

of the first resonance, $\Delta(1232)$, many models are well-developed and are successful in describing the resonance spectrum quantitatively: MAID [1, 2, 3], SAID [4, 5, 6], and others [16, 17, 18]. One finds a substantial increase in uncertainties for masses and hadronic and electromagnetic couplings of higher resonances where resonant and non-resonant channels compete. An increase in the total center-of-mass (CM) energy W is followed by an increase in the number of coupled channels, which have to be related via unitarity. At this point, even the use of all available data on the resonance production cannot resolve the difficulties of the model approaches in particular for $W > 1.6$ GeV. To constrain these hadronic and EM couplings, there is currently an intensive worldwide effort to simultaneously study all decay channels produced in photo- and electromagnetic excitation of the nucleon [19, 20].

The results for reaction (2) will be presented in another paper. In this paper we present cross-section measurements of reaction (1) made in Hall A of the Thomas Jefferson National Accelerator Facility (JLab) at an incident electron energy 4 GeV and fixed four-momentum transfer squared $Q^2 = 1.0$ GeV 2 . The scattered electron and proton (momenta k' and p' respectively) are detected at laboratory angles θ_e and θ_p , and the neutral pion is reconstructed using a missing-mass technique. The missing mass squared is expressed as $M_X^2 = (k + p - k' - p')^2$ where k and p are the momentum of the initial electron and proton, respectively. The relevant kinematical variables are shown in Fig. 1.

The kinematics were further restricted to forward detection (relative to the virtual photon momentum vector) of the recoil proton (backward CM π^0 emission). This reaction has been studied previously at the NINA electron synchrotron at a beam energy of 4 GeV [21], at DESY at 2.7 and 3.2 GeV [22, 23, 24, 25, 26] and, recently, in Hall C [27] and Hall B [28, 29, 30] experiments at JLab.

Our results will be presented as the conventional center of mass photo-production cross section, where the photon flux factor Γ (Hand convention) is introduced in the one-photon-exchange approximation:

$$\frac{d^5\sigma}{dk'd\Omega_e d\Omega_{\pi}^*} = \Gamma \frac{d^2\sigma}{d\Omega_{\pi}^*}, \quad (3)$$

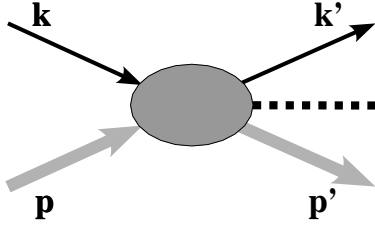


FIG. 1: Definition of kinematic variables for reaction (1). Thin lines represent the incident and outgoing electrons, and thick lines correspond to the target and recoil protons. The dashed line stands for the produced neutral pion.

$$\Gamma = \frac{\alpha}{2\pi^2} \frac{k'}{k} \frac{W^2 - M_p^2}{2M_p \cdot Q^2} \frac{1}{1 - \epsilon}, \quad (4)$$

where Ω_e is the differential solid angle for the scattered electron in the LAB frame, Ω_π^* is the differential solid angle for the proton in the final pion-proton CM frame, M_p is the proton mass, α is the fine-structure constant, and ϵ is the virtual photon polarization:

$$\epsilon = \frac{1}{1 + 2\frac{(\vec{k} - \vec{k}')^2}{Q^2} \tan^2(\frac{\theta_e}{2})}. \quad (5)$$

In the following, θ^* is defined as the polar angle between the virtual photon and the pion in the pion-proton center of mass system. ϕ is the azimuthal angle between the leptonic and the hadronic planes (ϕ is taken equal to 0 when the pion is emitted in the half plane containing the outgoing electron). This two-fold differential cross section can be written as a function of transverse, longitudinal and interference parts $d^2\sigma_T$, $d^2\sigma_L$, $d^2\sigma_{TL}$ and $d^2\sigma_{TT}$, that only depend on W , Q^2 and θ^* :

$$\begin{aligned} \frac{d^2\sigma}{d\Omega_\pi^*} = & \frac{d^2\sigma_T}{d\Omega_\pi^*} + \epsilon \frac{d^2\sigma_L}{d\Omega_\pi^*} + \sqrt{2\epsilon(1+\epsilon)} \frac{d^2\sigma_{TL}}{d\Omega_\pi^*} \cos\phi \\ & + \epsilon \frac{d^2\sigma_{TT}}{d\Omega_\pi^*} \cos 2\phi. \end{aligned} \quad (6)$$

In the rest of the paper, we will refer to the differential cross sections as $\sigma_T + \epsilon \sigma_L$, σ_{TL} and σ_{TT} .

II. EXPERIMENTAL PROCEDURE AND DATA ANALYSIS

A. Apparatus

The experiment was performed using a continuous electron beam with an energy of 4032 MeV incident on a liquid hydrogen target. The scattered electron and the recoil proton were detected in coincidence in two high-resolution spectrometers (HRSE and HRSR). Figure 2 is

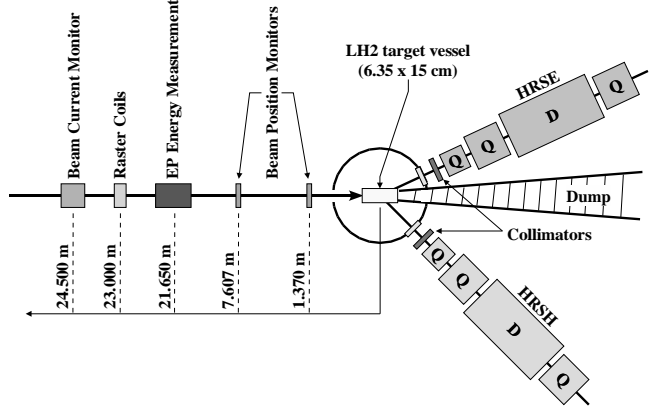


FIG. 2: Layout of the Hall A experimental setup.

a top view of the experimental set-up and the relevant components. More information on the Hall A setup is available in [31].

1. Electron beam

Typical beam intensities ranged from 60 to 120 μA ; they were continuously monitored during data taking using two resonant-cavity beam-current monitors (BCM) [32]. An absolute calibration of the BCMS was performed at least once per day by employing an Unser transformer [33]. The measured standard deviation and drift of the BCM ensured a stability of the current measurement of $\pm 0.3\%$ over the entire experiment. In order to avoid local boiling of hydrogen in the target, the incident beam was rastered (± 4 mm horizontal and vertical) with two asynchronous horizontal and vertical magnetic coils (≈ 20 kHz) located 23 m upstream of the target. The instantaneous position of the beam at the target was determined with an accuracy of about 100 μm with a pair of beam position monitors (BPM) located at 7.607 m and 1.370 m upstream of the target [34]. Each BPM is a resonant cavity with a set of four antenna wires parallel to the beam axis. The difference between the signals on opposing wires is proportional to the beam position.

2. Target

The liquid hydrogen target material was contained in a cylindrical aluminium vessel (0.0635 m diameter and 0.15 m long along the beam axis — see Fig. 2). The target wall thickness was 175 μm . The entrance and exit windows were 71 and 94 μm thick, respectively [35].

The target itself is located inside a cylindrical aluminium scattering chamber connected to the beamline vacuum. The scattering chamber was equipped with two 400 μm aluminium exit windows, each facing a spectrom-

eter.

The working temperature and pressure of the hydrogen loop (19.0 K and 25 psia) give a nominal density ρ_0 of 0.0723 g/cm³.

The data taken within 100 s after a substantial beam intensity variation (e.g. beam trips) were excluded from the analysis to avoid instabilities in the target density.

3. Magnetic spectrometers

The two high resolution spectrometers (HRS) of QQDQ type are of identical conception. Their main characteristics include a central momentum range from 0.3 to 4.0 GeV/c, and a nominal acceptance of $\pm 4.5\%$ in momentum, ± 65 mrad in vertical angle, ± 30 mrad in horizontal angle, and ± 5 cm in target length (transverse to the spectrometer axis). The magnetic dipole in each spectrometer deflects the particle trajectories in the vertical plane by 45° onto a 2 m long focal plane. The acceptance is defined in part by a tungsten collimator positioned at 1.109 m and 1.100 m (respectively for the electron and hadron arms) from the target, and by the apertures of the magnets. The vacuum box of the spectrometer is closed by a 178 μm Kapton entrance window and a 100 μm titanium exit window. In this experiment, the spectrometers were positioned with an absolute angular accuracy of 0.5 mrad.

4. Detectors

The detector package of each spectrometer is shown in Fig. 3. It includes:

- Two vertical drift chambers (VDC) [36], spaced by 50 cm, to define the trajectories of the charged particles; each VDC is equipped with two wire planes, to measure the intercepts and slopes of each trajectory in two perpendicular planes; charged particles passing within the acceptance of the spectrometer cross the plane of the chambers triggering from 3 to 5 sense wires. Each sense wire starts an updating time to digital converter (TDC) which is stopped by the acquisition trigger.
- Two scintillator planes S_1 and S_2 each consisting of 6 plastic scintillator paddles. The S_1 paddles are 29.3 cm (dispersive) by 36.0 cm (transverse) and the S_2 paddles are 37.0 cm (dispersive) by 60.0 cm (transverse). In both planes the paddles overlap by 0.5 cm. Each paddle is viewed by 2 photomultiplier tubes (PMT) at opposite ends.
- A gas Cherenkov counter (filled with CO₂) viewed by 10 PMTs. Only the Cherenkov counter of the electron spectrometer was used in this experiment.

Each PMT output is fed to an amplitude to digital converter (charge integrating ADC) and to a discriminator.

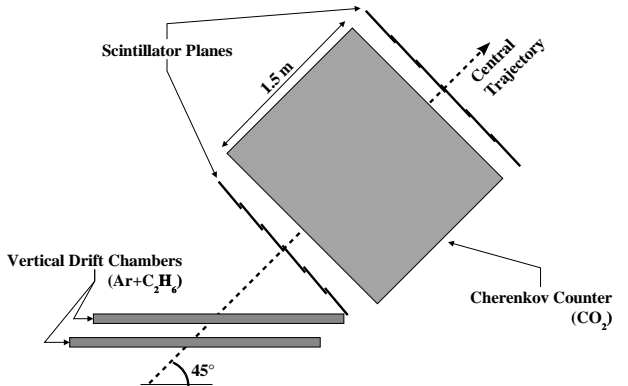


FIG. 3: HRSE detector package. The vertical drift chambers as well as the trigger scintillator hodoscopes are common to both spectrometers.

Each discriminator signal is sent to a TDC and to the fast electronics logic.

5. Trigger electronics and data acquisition

The fast electronics logic defines several trigger signals for the data acquisition system (DAQ) using the CEBAF Online Data Acquisition (CODA v1.4) [37]:

- T1 (T3) corresponds to a good electron (proton) event. It requires a coincidence between a paddle i of the S_1 plane and a paddle j of the S_2 plane within the directivity limits of the spectrometer ($|i - j| \leq 1$). Each paddle event (S_1 or S_2) requires a coincidence between the two PMTs at the end of each paddle.
- T2 (T4) defines a deficient electron (proton) event. This requires that either the $S_1 \cap S_2$ coincidence is not within the directivity limits ($|i - j| > 1$) or that only one scintillator plane fires. For the T2 trigger, if only one scintillator plane has a two-ended coincidence, the trigger logic requires a coincidence with the gas Cherenkov counter signal.
- T5 is the main trigger and is defined by a coincidence of T1 and T3 within 100 ns.

Although all triggers can fire the DAQ, T5 has priority while other triggers are prescaled. This fraction is set using prescale factors (PS₁, PS₂, PS₃ and PS₄). The encoding of the analog signals and the transfer of the digitized signal to the computer buffers takes $\sim 700 \mu\text{s}$. When the DAQ is triggered, it forbids any other trigger until the first is processed. This induces acquisition dead times up to 30 % for some high counting rate conditions. The number of events for every trigger type is recorded by a running scaler, which is read and logged by the DAQ every 10 seconds.

B. Data taking geometry

Data were taken at nine spectrometer angle and momentum settings (numbers 4-12 in Table I), covering the entire resonance region, i.e. a total CM energy W varying between pion threshold and 2.0 GeV. W is the invariant mass of the $(\gamma^* p)$ system, $W = \sqrt{(k - k' + p)^2}$. The acceptance in θ^* was centered around 180° . Complementary measurements (settings #1, 2, 3 in Table I) were included in order to increase the statistical accuracy around the pion production threshold. Additional $H(e, e')p$ elastic scattering measurements with a sieve slit (and both spectrometers tuned to electrons) and Al, C(e, e') X quasi-elastic measurements with an array of foil targets served for calibration of detectors and spectrometer optics. The relevant information on production data is summarized in Table I.

TABLE I: Kinematical settings used for the π^0 data taking. The incident electron energy was 4032 MeV (discussed in Section II C 1). The values shown in the table are the central values within the acceptance.

Setting number	W_{nom} (GeV)	k'_{nom} (GeV/c)	$(\theta_e)_{\text{nom}}$ (°)	p'_{nom} (GeV/c)	$(\theta_p)_{\text{nom}}$ (°)
1	1.180	3.433	15.43	1.187	-50.00
2	1.178	3.433	15.43	1.187	-48.50
3	1.177	3.433	15.43	1.187	-46.50
4	1.217	3.282	15.77	1.323	-45.41
5	1.252	3.176	16.04	1.418	-41.67
6	1.326	3.043	16.39	1.539	-37.49
7	1.431	2.909	16.76	1.662	-33.82
8	1.526	2.776	17.16	1.787	-30.60
9	1.613	2.642	17.87	1.914	-27.75
10	1.690	2.482	18.15	2.067	-24.75
11	1.795	2.269	18.99	2.274	-21.34
12	1.894	2.056	19.96	2.482	-18.46

C. Data analysis

1. Method

The data analysis procedure includes several passes. In a first step, we reject any sequence of CODA events collected when one of the stability requirements fails: beam intensity or position, spectrometer magnetic elements, etc.

Next, the Hall A analyzer ESPACE (Event Scanning Program for Hall A Collaboration Experiments) [38] is used to construct the trajectory of the particles in the spectrometer focal plane from the VDC data : two position coordinates X_{fp} and Y_{fp} and two cartesian angles ϕ_{fp} and θ_{fp} .

Then, using the beam position information at the target and the database for the spectrometers optics, ESPACE reconstructs the entire kinematics of the electron

and the proton at the vertex, as well as the interaction point. This database has been optimized for the kinematical settings of this experiment [39]. Both particles at the vertex are described with four spectrometer variables : the transverse coordinate Y_{tg} , the two cartesian angles ϕ_{tg} and θ_{tg} , and the relative momentum

$$\delta k' = \frac{k' - k'_{\text{nom}}}{k'_{\text{nom}}} \text{ (electron)} \quad (7)$$

$$\delta p' = \frac{p' - p'_{\text{nom}}}{p'_{\text{nom}}} \text{ (proton).} \quad (8)$$

The dispersive coordinate X_{tg} is deduced from the beam information. The energy loss in the target and spectrometer windows is also taken into account.

At this stage, the position and the shape of the missing mass squared M_X^2 distribution are indicators of how the positioning of the spectrometers and the beam are under control. The missing mass resolution was optimized by varying the beam energy, the vertical angle θ_{tg} of the electron arm, the horizontal angles of both arms ϕ_{tg} , and the calibration of the vertical beam raster amplitude at the target. The result of this optimization yields an average correction for the beam energy of -13 MeV to the nominal value of 4045 MeV, with a dispersion of ± 3 MeV, varying from one run to another. A similar procedure based on the horizontal position of the reconstructed vertex is used to determine the calibration of the horizontal raster amplitude and the horizontal mispointing of the spectrometers.

2. Simulation and radiative corrections

We use a detailed simulation [40] which takes into account all processes that affect the characteristics of the experimental data. Indeed, these data stem from a convolution of the “ideal” events defined at the vertex with a number of processes that influence the incident beam and the outgoing (detected) particles. The simulation incorporates the beam profile distribution, collisional energy losses, multiple scattering, internal and external bremsstrahlung and radiative corrections [41], as well as other resolution effects (*e.g.* from optics and detector resolution). The spectrometers acceptance is simulated with a model based on the optical design of the spectrometer and field maps of the magnets [39]. In order to reconcile the results of the simulation with the data, an additional smearing had to be introduced. This correction depends on the data-taking geometry and is listed in Table II.

Events are generated according to a model cross section $d\sigma_{\text{model}}$. In a first step, $d\sigma_{\text{model}} = \text{MAID2000}$ [1, 2] (this is discussed in Section III). In a second step a *local fit* based on MAID2003 [3] is performed on our data (Section III B), and in a third step a dependence on Q^2 is added based on our experimental results (Section IV).

TABLE II: Additional Gaussian resolution smearing at each experimental setting (rms) for reconstructed variables at the target.

Setting number	electron			proton		
	θ_{tg} (mrad)	Y_{tg} (mm)	$\delta p'$ (10^{-4})	ϕ_{tg} (mrad)	θ_{tg} (mrad)	Y_{tg} (mm)
1	1.00	.00	2.00	1.00	2.00	.30
2	1.00	.00	2.00	1.00	2.00	.30
3	1.00	.00	2.00	1.00	2.00	.30
4	1.35	.30	2.75	1.35	2.75	.30
5	1.45	.42	3.00	1.45	3.00	.42
6	1.80	.33	3.60	1.80	3.60	.33
7	1.65	.00	3.30	1.65	3.30	.00
8	1.80	.66	3.60	1.80	3.60	.66
9	1.80	.66	3.60	1.80	3.60	.66
10	1.80	.66	3.60	1.80	3.60	.66
11	1.80	.66	3.60	1.80	3.60	.66
12	1.50	.66	3.00	1.50	3.00	.66

Our procedure for radiative corrections has been actually developed for process (2) following the exponentiation method of [41], and has been applied in the same way to process (1). In this method, radiative corrections are implemented in two parts according to the source of photon radiation. The first contribution is the acceptance-dependent part of the internal and external bremsstrahlung from the electron lines, and as such it is included in the simulation [40]. This reproduces the radiative tail in the missing mass squared spectrum (see Fig. 5). The second contribution is expressed as a constant factor equal to 0.93 at $Q^2 = 1.0$ GeV 2 applied to the cross section. The systematic error associated with the radiative corrections is taken equal to $\pm 2\%$ [41].

3. π^0 event selection

The following criteria and cuts have been applied to properly select the π^0 events :

- A suitable coincidence timing window, as illustrated in Fig. 4.
- A directivity cut applied on the particle's position in the collimator plane at the entrance of each spectrometer : ± 2.9 cm in horizontal and ± 5.8 cm in vertical (This corresponds to 87% of the total geometrical acceptance of the 6 msr collimator).
- An acceptance cut defined for both arms by :

$$\delta k'(p') \leq A \pm B * \phi_{tg} + C * Y_{tg}^2 \quad (9)$$

with $A = 0.17$, $B = 6.0$ rad $^{-1}$ and $C = -23.15$ m $^{-2}$. This cut approximates the dipole aperture and was used to symmetrise the acceptance which is not completely defined by the collimator alone.

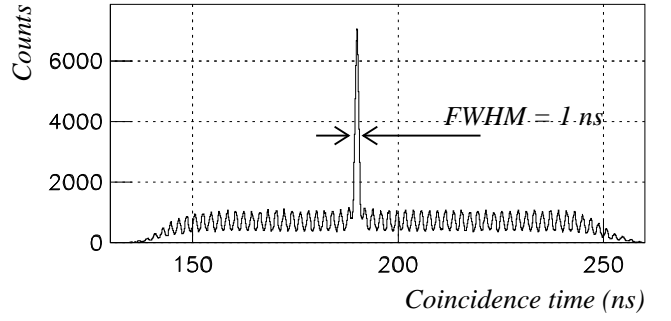


FIG. 4: Coincidence time for setting #7. The time is corrected for the path length in the spectrometer and for the proton velocity. The fine structure in the time spectrum is due to the 500 MHz structure of the beam.

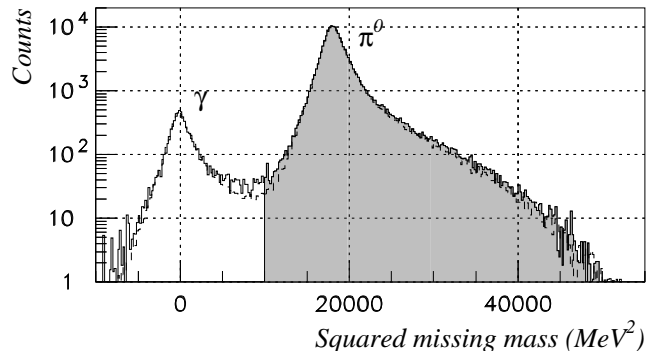


FIG. 5: Experimental distribution of the missing mass squared (solid) and the corresponding simulated spectrum (dashed line) obtained by registering the process $p(e, e'p)X$. The peak around zero corresponds to events originating from reaction (2). The maximum of the second peak is at the pion mass squared $m_{\pi^0}^2 = 18.2 \cdot 10^3$ MeV 2 as to be expected if events originated from reaction (1). The colored region represents the event distribution within the selection window for process (1).

- An acceptance cut defined in both arms in the plane (Y_{tg}, ϕ_{tg}). This cut has an hexagonal shape and tends to reproduce the quadrupoles apertures. More information on this cut is given in [42].
- A cut on the horizontal transverse distance d between the beam and the reconstructed vertex (using both arms) :

$$|d| < 0.003 \text{ m} \quad (10)$$

- A selection window on the missing mass squared : $10000 < M_x^2 < 50000$ MeV 2 . The lower boundary of the selection window serves to suppress the yield from reaction (2) which is manifest as a peak at $M_x^2 = 0$ in Fig. 5.

D. Cross sections evaluation

1. Extraction method

In the present analysis, a typical experimental bin of phase space is defined in the five kinematic variables $Q^2, W, \epsilon, \cos \theta^*, \phi$, and the missing mass squared M_X^2 . The number of events in each bin is the product of the integrated luminosity \mathcal{L} and the convolution of the physical cross section with resolution effects over all the experimental acceptance. Let N_i denote the number of counts observed in bin i , and \mathcal{K}_i the experimental resolution and acceptance function of the same bin. Then

$$N_i = \mathcal{L} \int [d^6\sigma \otimes \mathcal{K}_i]. \quad (11)$$

The number of events simulated in the given bin i , $N_i^{(s)}$, is defined by the simulated luminosity \mathcal{L}_s times the five-fold differential Born (non-radiative) cross section $d^5\sigma_s$ depending on variables $Q^2, W, \epsilon, \cos \theta^*$ and ϕ convoluted with the radiative process and the experimental resolution. If we denote the contribution of the radiative processes (including internal and external bremsstrahlung) by $d\mathcal{R}_s$, and the simulated resolution response and acceptance of bin i by $\mathcal{K}_i^{(s)}$, the simulated number of events is then :

$$N_i^{(s)} = \mathcal{L}_s \int [d^5\sigma_{\text{model}} \otimes d\mathcal{R}_s \otimes \mathcal{K}_i^{(s)}]. \quad (12)$$

If the processes described by Eq. (12) are correctly taken into account in the simulation, then, assuming that the relative variation of the true cross section and the simulated one around a point $\mathcal{P}_0 = (W, Q^2, \epsilon, \cos \theta^*, \phi)$ are the same :

$$\frac{d\sigma(\mathcal{P}) - d\sigma(\mathcal{P}_0)}{d\sigma(\mathcal{P}_0)} = \frac{d\sigma_{\text{model}}(\mathcal{P}) - d\sigma_{\text{model}}(\mathcal{P}_0)}{d\sigma_{\text{model}}(\mathcal{P}_0)}, \quad (13)$$

we arrive at the experimental differential cross section at point \mathcal{P}_0 :

$$d^5\sigma(\mathcal{P}_0) = \frac{\mathcal{L}_s}{\mathcal{L}} \times \frac{N_i}{N_i^{(s)}} \times d^5\sigma_{\text{model}}(\mathcal{P}_0). \quad (14)$$

These assumptions are verified *a posteriori* by observing a good agreement between the experimental and simulated distributions (e.g. missing mass spectra in Fig. 5). The size of the bins is only constrained by the magnitude of the resolution and radiative effects, and by the variation of the model cross section $d\sigma_{\text{model}}$. In this analysis, we choose the point \mathcal{P}_0 to lie at the center of each bin.

2. Adjustment of the model parameters

The procedure described by Eq. 13 to evaluate the experimental cross section relies heavily on the accuracy of

the simulation of the true cross section inside each bin by the model cross section $d\sigma_{\text{model}}$. Thus, it is imperative to employ a realistic model cross section in the Monte Carlo simulation.

At the start of the analysis we used in the simulation and, consequently, in the determination of the experimental cross section, the MAID2000 model (see Section III A). It was found at this stage of the analysis that the model cross section departs from the measured one, especially for the second and third resonance regions. In particular we observed strong differences in the W, Q^2 and ϕ dependences of the cross section which motivated an adjustment of the model parameters (see Section III B).

At the second step of the iteration the experimental cross section was evaluated by employing the model version MAID2003 with adjusted parameters (*local fit*). This adjustment did not involve model parameters responsible for the Q^2 dependence because the present data comprise a rather limited Q^2 interval.

In a last step we used our experimental results to obtain an estimation of the Q^2 dependence. Another iteration was performed afterwards by including in the simulation the new Q^2 dependence (see Section IV). The final results are presented in Sections IV and V.

3. Corrections and systematic errors

In the extraction of the cross section values, a number of corrections have to be taken into account. For each correction, the residual systematic error was evaluated. All relevant quantities are given in Table III.

TABLE III: Correction and systematic error evaluation

Source	Correction	Induced error on σ
Trigger efficiency	1-10 %	$\pm 0.0 \%$
Acquisition dead time	0-30 %	$\pm 0.0 \%$
Electronics dead time	2.5-4.5 %	$\pm 0.1 \%$
Tracking efficiency	3.0-8.0 %	$\pm 0.5 \%$
Optics		$\pm 1.2 \%$
Acceptance		$\pm 2.0 \%$
Target boiling		$\pm 1.0 \%$
Proton absorption correction	1-3 %	$\pm 0.1 \%$
Radiative corrections		$\pm 2.0 \%$
Photon contamination	1.0 %	$\pm 0.0 \%$
Quadratic sum		$\pm 3.3 \%$

The trigger efficiency correction $E_{1,2}(x, y)$ is calculated run by run for each scintillator plane (1 and 2), locally in longitudinal (x) and transverse (y) directions. The VDCs determine the particle's track location in the scintillator. For this efficiency study, a stringent event selection in the four planes of the VDCs is applied. The efficiency correction factor is then (for the electron arm) :

$$E_{1,2}(x, y) = 1 + \quad (15)$$

$$\frac{N(T_2 \cdot \overline{S_{1,2}}) \times PS_2}{N(T_5) + N(T_1) \times PS_1 + N(T_2 \cdot \overline{S_{1,2}}) \times PS_2}.$$

Here, $N(T_2 \cdot \overline{S_{1,2}})$ is the number of T2 trigger events tracked by the VDCs to the (X_{fp}, Y_{fp}) area, but with no $S_1 \cap S_2$ scintillator coincidence. A similar procedure is applied for the hadron arm with the T4 triggers. The correction is of the order of 2 % for the electron arm, and less than 1% for the hadron arm. The accuracy on this correction is governed by the number of T2 and T4 triggers, and is of the order of 1–5% of the inefficiency. This induces no appreciable systematic error in the final result.

The dead-time correction factor of the acquisition system is the ratio of the number of events measured by the scaler associated to trigger T5 to the total number of coincidence events found in each run. It ranges from 0 to 30 % and the associated error is negligible.

The dead time associated with the electronics is defined by the setup and depends directly on the beam intensity. It is evaluated for each run from the singles rate of each discriminator associated with the scintillator paddles and electron Cherenkov. Typically, the correction is 2.5% at the $\Delta(1232)$ resonance, and 4.5% for the highest W setup. The induced systematic error is negligible.

The intrinsic efficiency of the VDCs is determined by the efficiency of each sense wire. A good track requires a signal from at least 3 wires in each plane. The fact that a typical track intercepts five cells in each wire plane makes the VDCs global inefficiency negligible.

The tracking efficiency is affected by accidental hits, caused by background events, which can prevent the algorithm from reconstructing the good track. Thus, a noticeable fraction of the events has more than one reconstructed track in the VDCs. These events are rejected in the analysis and the luminosity is decreased in proportion. Also this correction depends strongly on the setup configuration and on the beam current, and varies between 3% and 8%. The systematic error in this correction is estimated to be 10% of the correction.

Independent of the uncertainty in the total acceptance of the HRS pair, we have a cross section uncertainty from the imperfect knowledge of the spectrometer optics. We subdivide the acceptance into bins in the physics variables Q^2 , W , M_X^2 , $\cos\theta^*$, and ϕ . The precise volume of each bin is subject to uncertainties due to *local* variations in the average reconstruction of vertex variables. We estimate these uncertainties from the rms deviations between the positions of the sieve slit holes (at the entrance of each spectrometer) and the mean reconstructed position of these holes. Local variations in the calibration of vertex positions along the beam line influence the luminosity, which is proportional to the effective target length viewed by the HRS pair. We estimate the uncertainty in the effective target lengths from the deviations between the positions of a set of seven reference foil targets and their reconstructed positions. The sieve slit holes are on a square grid of spacing 25 mm vertical and

12.5 mm horizontal. The seven targets were located at 0, ± 20 , ± 50 , and ± 75 mm along the beam axis. In the electron arm, the rms deviations of the mean reconstructed values are 0.065 mm and 0.050 mm, for the vertical and horizontal sieve slit holes, respectively, and 0.145 mm for the target foils along the beam axis. The same values for the hadron arm are 0.097 mm, 0.027 mm, and 0.220 mm. Dividing the rms variations by the respective spacings in the vertical and horizontal sieve slit holes and the reference targets, we obtain the contributions to the cross section uncertainties arising from local variations in optics. Adding all contributions in quadrature yields an uncertainty of $\pm 1.2\%$. This is the optics uncertainty in Table III.

We have performed a set of acceptance cuts to improve the agreement between the experiment and the simulation (see Section II C 3). The uncertainty associated with possible residual discrepancies is estimated to be $\pm 2\%$.

The beam current and its variation can lead to target density corrections to the luminosity. The beam was rastered over an area proportional to the beam current, and equal to $8 \times 8 \text{ mm}^2$ at $100 \mu\text{A}$ to minimize any effect of hydrogen boiling. In analyses of single-arm elastic data, no correlation was observed between the target density and the beam current [43], within $\pm 1\%$.

From the analysis of the single-arm elastic data, it was also concluded that the target impurity is negligible, i.e. $\leq 0.02\%$.

A correction was also evaluated for lost recoil protons, either from interactions with the liquid hydrogen target material or in the different windows; its value equals 1% near the pion production threshold and reaches about 3% at the highest W .

The error associated with the radiative correction is $\pm 2\%$. This matter has been discussed in Section II C 2.

Finally, at low W , the contribution of reaction (2) is not negligible in the selected window in missing mass squared. A correction has been made to subtract the photon events located below the π^0 peak (see Fig. 5) ; it does not induce any further systematic error.

The total error evaluated as a quadratic sum of all the contributions amounts to $\pm 3.3\%$. This total error will be added quadratically to the model dependence error discussed in Section V.

III. STUDY OF THE W , θ^* AND ϕ DEPENDENCES

A. Excitation curves and angular distributions

The method presented in Section II D was applied to produce the two-fold differential cross section as a function of W , Q^2 , $\cos\theta^*$ and ϕ . The cross section is evaluated in $50 \times 1 \times 4 \times 12$ kinematical intervals chosen as shown in Table IV. Figure 6 shows a sample excitation curve for $Q^2 = 1.0 \text{ GeV}^2$, $\cos\theta^* = -0.975$ and $\phi = 75^\circ$.

TABLE IV: Binning intervals for each variable. Note that the analysis of the Q^2 dependence discussed in Section IV required splitting of the Q^2 range into 6 intervals as well as a wider binning in W and $\cos\theta^*$ (these values are indicated in parenthesis).

Variable	Range	Number of intervals	Interval width
W	$[1.00;2.00]$ GeV	50(10)	0.02(0.1) GeV
Q^2	$[0.85;1.15]$ GeV 2	1(6)	0.3(0.05) GeV 2
$\cos\theta^*$	$[-1;-0.8]$	4(1)	0.05(0.2)
ϕ	$[0;360]$ $^\circ$	12	30 $^\circ$

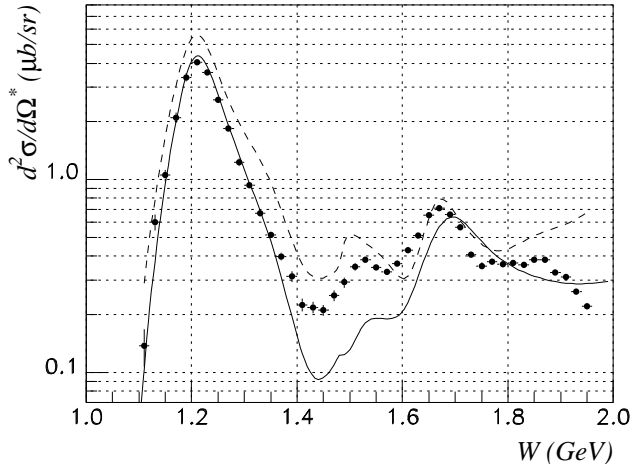


FIG. 6: Excitation curve for $\gamma^* p \rightarrow p\pi^0$ at $Q^2 = 1.0$ GeV 2 , $\cos\theta^* = -0.975$, and $\phi = 75^\circ$. The full line corresponds to MAID2000 [1, 2] and the dashed line to SAID (*NF18K solution*) [4].

The data integrated over the whole Q^2 range yield the cross section as a function of ϕ for each W and $\cos\theta^*$ interval. As an example, we present in Fig. 7 the azimuthal distributions for four points in W .

The corresponding cross-section data evaluated in the framework of the MAID2000 model [1, 2] demonstrate a good agreement with the results obtained in the $\Delta(1232)$ region. The agreement deteriorates as W increases (Figs. 6 and 7).

For each bin in W and $\cos\theta^*$, we obtain the separated cross sections $\sigma_T + \epsilon \sigma_L$, σ_{TL} and σ_{TT} by fitting Eq. (6) to the data in 12 bins in ϕ (Fig. 7). In the procedure of minimization only the statistical errors are used.

There exists another well-developed technique for describing pion electroproduction over the whole resonance region — the SAID analysis [4, 5, 6]. SAID employs the regularly updated compilation of available data for photo- and electro-production reactions to constrain a certain set of parameters in an energy-dependent multipolar fit. The output of such fit corresponding to the *NF18K solution* is displayed in Fig. 6. Although the *NF18K solution* overpredicts our data from threshold to

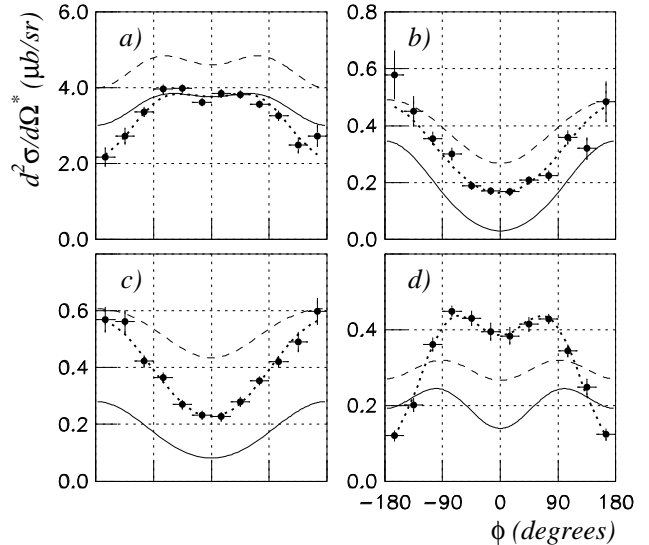


FIG. 7: Azimuthal angular distributions for $\gamma^* p \rightarrow p\pi^0$ at $Q^2 = 1.0$ GeV 2 , $\cos\theta^* = -0.975$ for different points in W : 1230 MeV — a), 1410 MeV — b), 1510 MeV — c) and 1610 MeV — d). The solid curve corresponds to MAID2000 [1, 2] and the dashed line to SAID (*NF18K solution*) [4]. The dotted line approximating the data points is obtained from the fit of Eq. (6).

$W = 1.6$ GeV, the general trends of the cross section are well reproduced (Figs. 6, 7). The agreement between the SAID model and our data is significantly improved after the data is added to the world database (see Section III C).

B. Amplitude Analysis with MAID

With our complete dataset of 363 data points in three observables and three values of pion emission angle we performed a data analysis using the unitary isobar model MAID2000 [1, 2]. This model is based on the evaluation of a nonresonant background described by Born terms and vector meson exchange, and a resonant part modeled with Breit-Wigner functions for all four star nucleon resonances below $W = 2$ GeV,

$$t_{\gamma\pi}^\alpha = v_{\gamma\pi}^{bg,\alpha} (1 + it_\pi^\alpha) + t_{\gamma\pi}^{BW,\alpha} e^{i\phi_\alpha}. \quad (16)$$

Both parts are individually unitarized. For the background part this is done in the usual K-matrix approximation and for the resonance part by including an energy dependent unitarization phase ϕ_α . The background and the hadronic parameters of the resonances are fixed, leaving only the electromagnetic couplings of the N^* 's and Δ 's as free parameters. For electroproduction these are electric, magnetic and longitudinal couplings that can be expressed in terms of the helicity amplitudes $A_{1/2}$, $A_{3/2}$ and $S_{1/2}$. They are defined at the resonance position $W = M_R$ and are related to the transition form factors.

In MAID2000 the Q^2 dependence of these couplings is modeled by semi-phenomenological form factors. In the MAID2003 calculation [3], it has a phenomenological form fitted to all existing electroproduction data (*global fit*). Since our data are taken in a narrow interval around $Q^2 = 1.0$ GeV 2 , the current analysis will be a fixed- Q^2 analysis (*local fit*).

In our analysis, for the 13 nucleon resonances below $W = 2$ GeV, we fix the parameters of five from the results of the *global fit*, and adjust the parameters of the remaining eight resonances. These are the $P_{33}(1232)$, $P_{11}(1440)$, $D_{13}(1520)$, $S_{11}(1535)$, $S_{31}(1620)$, $S_{11}(1650)$, $F_{15}(1680)$ and $D_{33}(1700)$, giving a total of 20 free parameters. In order to estimate the model uncertainties in our fit, we successively fixed individual resonance parameters to the values of the *global fit*, and investigated the fluctuations in the remaining parameters. In Table V we give the result of our *local fit* for the five resonances for which the parameters are found to reasonably fluctuate around initial values. The $S_{31}(1620)$, $S_{11}(1650)$, and $D_{33}(1700)$ are excluded from the table, as their parameters could not be constrained in the present analysis. The main reason for this is a restricted angular range of our dataset, which is confined to backward angles. Furthermore, by not including any world π^+ data, our fit is insensitive to isospin. Even so, our data show strong sensitivity to the resonances at large W . In Table V, we compare our MAID2003 [3] *local fit* with the default values of MAID2000. For the $\Delta(1232)$ resonance, we give in addition the $R_{EM} = E2/M1$ and the $R_{SM} = C2/M1$ ratios. Both MAID2003 values are consistent with the previous MAID2000 fits [1, 2]. The R_{SM} ratio is very well determined by σ_{TL} and tends to larger negative values at $Q^2 = 1.0$ GeV 2 in comparison to $Q^2 = 0$, while the R_{EM} ratio is loosely constrained. Furthermore, the model uncertainties are larger for latter value than for the $C2/M1$ ratio. From σ_{TL} we also find a large sensitivity to the S_{0+} amplitude of the $S_{11}(1535)$ resonance in the minimum around $W = 1500$ MeV.

C. New Solution from SAID Analysis

The predictions of the SAID analysis with the *NF18K solution* parameter set [4] are shown in Figs. 6 and 7. This is an extrapolation to the new kinematics of our experiment. When our data are included in the world dataset, a new SAID fit, *WI03K solution* [6] yields a much better fit, as shown in Fig. 8 and Fig. 10. We find a noticeable improvement in the region of the $P_{33}(1232)$ resonance, resulting from improved constraints on the Q^2 dependence of this resonance. Although σ_{TL} is under-fitted at the P_{33} , in general SAID *WI03K solution* gives an excellent description of σ_{TL} and σ_{TT} up to $W = 1.7$ GeV.

TABLE V: Transverse and longitudinal helicity amplitudes $A_{1/2}$, $A_{3/2}$ and $S_{1/2}$ for electromagnetic excitation of nucleon resonances off the proton at $Q^2 = 1.0$ GeV 2 in units of 10^{-3} GeV $^{-1/2}$. The default values of MAID2000 are compared to our MAID2003 *local fit*. The $R_{EM} = E2/M1$ and $R_{SM} = C2/M1$ ratios of the $\Delta(1232)$ are given in percentage. The errors given for the amplitudes are first the statistical errors of the fit and second the estimated model uncertainty. The errors of the ratios include both and are mainly model uncertainties.

N^*	MAID2000		MAID2003
	default values	<i>local fit</i>	
$P_{33}(1232)$	$A_{1/2}$	-75	$-70 \pm 1 \pm 2$
	$A_{3/2}$	-142	$-161 \pm 3 \pm 5$
	$S_{1/2}$	15	$17 \pm 1 \pm 2$
R_{EM}		-2.2	-6.4 ± 2.6
		R_{SM}	-6.5 ± 1.7
$P_{11}(1440)$	$A_{1/2}$	-61	$18 \pm 5 \pm 20$
	$S_{1/2}$	20	$19 \pm 3 \pm 10$
$D_{13}(1520)$	$A_{1/2}$	-69	$-77 \pm 7 \pm 20$
	$A_{3/2}$	38	$40 \pm 7 \pm 10$
	$S_{1/2}$	0	$-17 \pm 8 \pm 10$
$S_{11}(1535)$	$A_{1/2}$	67	$74 \pm 10 \pm 25$
	$S_{1/2}$	0	$-22 \pm 5 \pm 10$
$F_{15}(1680)$	$A_{1/2}$	-42	$-36 \pm 5 \pm 10$
	$A_{3/2}$	51	$31 \pm 10 \pm 10$
	$S_{1/2}$	0	$-22 \pm 5 \pm 10$

D. θ^* dependence

The kinematic restrictions of the present experiment allow us to reliably reconstruct the event distributions as a function of the pion angle θ^* in the interval $-1 \leq \cos\theta^* \leq -0.8$. The corresponding cross section is shown in Fig. 8 after optimization of the MAID and SAID parameters.

Overall, the relative shape in θ^* of the MAID2003 *local fit* compared to the experimental data is good for all bins in W .

IV. STUDY OF THE Q^2 DEPENDENCE

We considered the correlation between ϕ and Q^2 due to the acceptance as a possible source of systematic error. To minimize this effect, we need a more realistic Q^2 dependence in the model. To this end we first extract the experimental Q^2 dependence for each bin in W and, second, iterate the analysis using a model cross section $d\sigma_{\text{model}}$ that includes this dependence.

The cross section was evaluated by splitting our Q^2 range $[0.85, 1.15]$ GeV 2 into six intervals, integrating over $\cos\theta^*$ in the range $[-1.0, -0.8]$, and fitting the ϕ dependence of the cross section in a similar way to that described in Section III.

The Q^2 dependence of the cross section can be studied by fitting the following form to the partial $\sigma_T + \epsilon \sigma_L$ cross

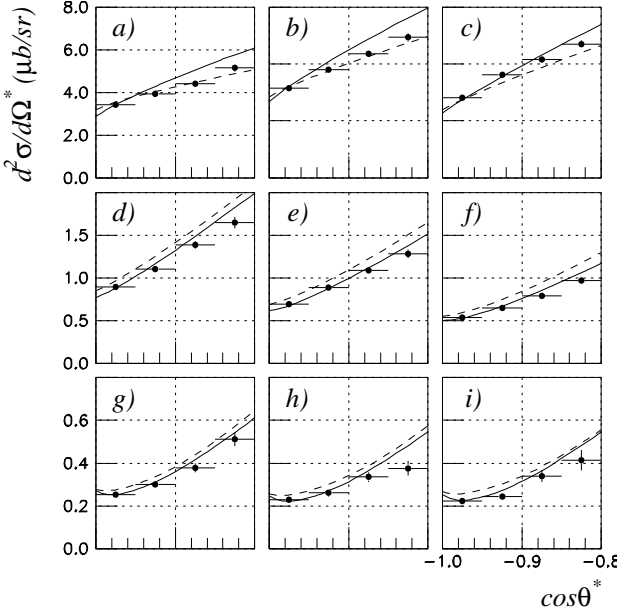


FIG. 8: The cross section of reaction (1) as a function of $\cos\theta^*$ obtained at $Q^2 = 1.0 \text{ GeV}^2$, $\phi = 75^\circ$ for different values of W : 1190 MeV — a), 1210 MeV — b), 1230 MeV — c), 1310 MeV — d), 1330 MeV — e), 1350 MeV — f), 1410 MeV — g), 1430 MeV — h) and 1450 MeV — i). In all plots, $-1.0 \leq \cos\theta^* \leq -0.8$. The solid curve depicts the MAID2003 *local fit* and the dashed line to the SAID *WI03K solution* [6].

section :

$$d\sigma(W, Q^2) = d\sigma(W, Q^2 = 1 \text{ GeV}^2) \cdot e^{-b_{\text{exp}} \cdot (1 \text{ GeV}^2 - Q^2)} \quad (17)$$

The resulting fit values for b_{exp} are displayed in Fig. 9. We performed a similar exercise on the cross section evaluated within the MAID2000 calculation and MAID2003 *local fit*. The resulting parameter $b_{\text{maid}}(W)$ is displayed in Fig. 9 respectively with a full and a dashed curve. While the overall ranges of variation of b_{exp} and b_{maid} are consistent, we observe a substantial discrepancy between the model and the data in the range of W from ~ 1.25 to $\sim 1.65 \text{ GeV}$.

The data obtained in the present analysis allow us to determine the Q^2 dependence of the partial cross section $\sigma_T + \epsilon \sigma_L$ over a wide range of W . In principle, it is also possible to study the Q^2 dependence of the partial cross sections σ_{TT} and σ_{TL} . However, such an analysis would require much more statistics for a meaningful interpretation.

The experimental Q^2 dependence of Eq. 17 is used in our final data analysis with the MAID2003 *local fit* parameters. In addition, we compute a systematic error associated with the Q^2 -dependent interpolation in the data analysis. This systematic error is evaluated from one half of the difference between the final analysis and the results obtained from the analysis using the MAID2003 *local fit* without additional Q^2 -dependence.

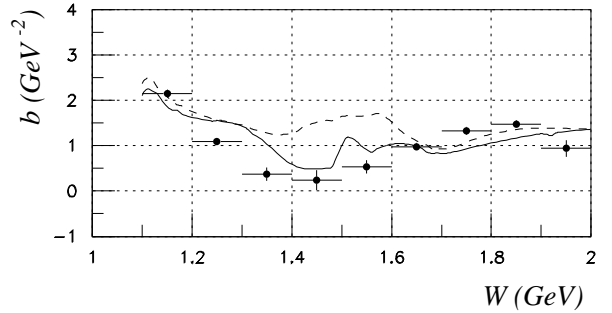


FIG. 9: Q^2 evolution of $\sigma_T + \epsilon \sigma_L$ evaluated at a central $Q^2 = 1.0 \text{ GeV}^2$ from the data points. The dashed and solid curve correspond to the MAID2000 and MAID2003 *local fit* calculations respectively. See text for definition of b .

V. DISCUSSION AND CONCLUSIONS

The final cross-section data are listed in Tables VI, VII and VIII [44]. The value of ϵ indicated in these tables corresponds to a fixed value of $k = 4032 \text{ MeV}$ within each considered interval in W .

Figure 10 presents the final cross sections $\sigma_T + \epsilon \sigma_L$, σ_{TL} and σ_{TT} as a function of W , evaluated at $\cos\theta^* = -0.975$.

The systematic errors obtained from the iterative procedure described in Section IV are added quadratically to the errors listed in Table III. The total systematic error is shown in Tables VI, VII, VIII and in Fig. 10. It is of the same order as the statistical error.

The parameter b_{exp} introduced in Section IV can be phenomenologically related with the scale parameter Λ , which determines the Q^2 dependence of hadronic form factors and resonance multipoles in the dipole approximation:

$$G_D(Q^2) = \frac{1}{(1 + Q^2/\Lambda^2)^2}, \quad (18)$$

Assuming that $d^2\sigma(Q^2) \sim (G_D(Q^2))^2$ one finds that $b_{\text{exp}} \approx 4/(Q^2 + \Lambda^2)$. Therefore $b_{\text{exp}} \rightarrow 0$ when the target is structureless ($\Lambda^2 \rightarrow \infty$), $b_{\text{exp}} \rightarrow 4/Q^2 = 4 \text{ GeV}^{-2}$ at $Q^2 = 1 \text{ GeV}^2$ in the case $\Lambda^2 \ll Q^2$. A standard fit to nucleon elastic form factors data yields $\Lambda^2 = 0.71 \text{ GeV}^2$, which at $Q^2 = 1 \text{ GeV}^2$ corresponds to $b_{\text{exp}} = 2.3 \text{ GeV}^{-2}$.

The range of observed variations of the parameter b_{exp} displayed in Fig. 9 lies essentially within the limits $0 < b_{\text{exp}} < 4 \text{ GeV}^2$. Thus, it is consistent with the Q^2 dependence of the dipole form factor discussed above.

While Eq. (18) provides a reasonable approximation for nucleon form factors in the range of Q^2 considered in this study, it is known to deviate [45] from the results obtained for the $\gamma N\Delta$ transition form factor $G_M^*(Q^2)$ which describes the dominant magnetic dipole excitation of the $\Delta(1232)$. In particular, $G_M^*(Q^2)$ falls off faster with Q^2 than the dipole form factor indicating a magnetic radius of the resonance state larger than that of the nucleon [27].

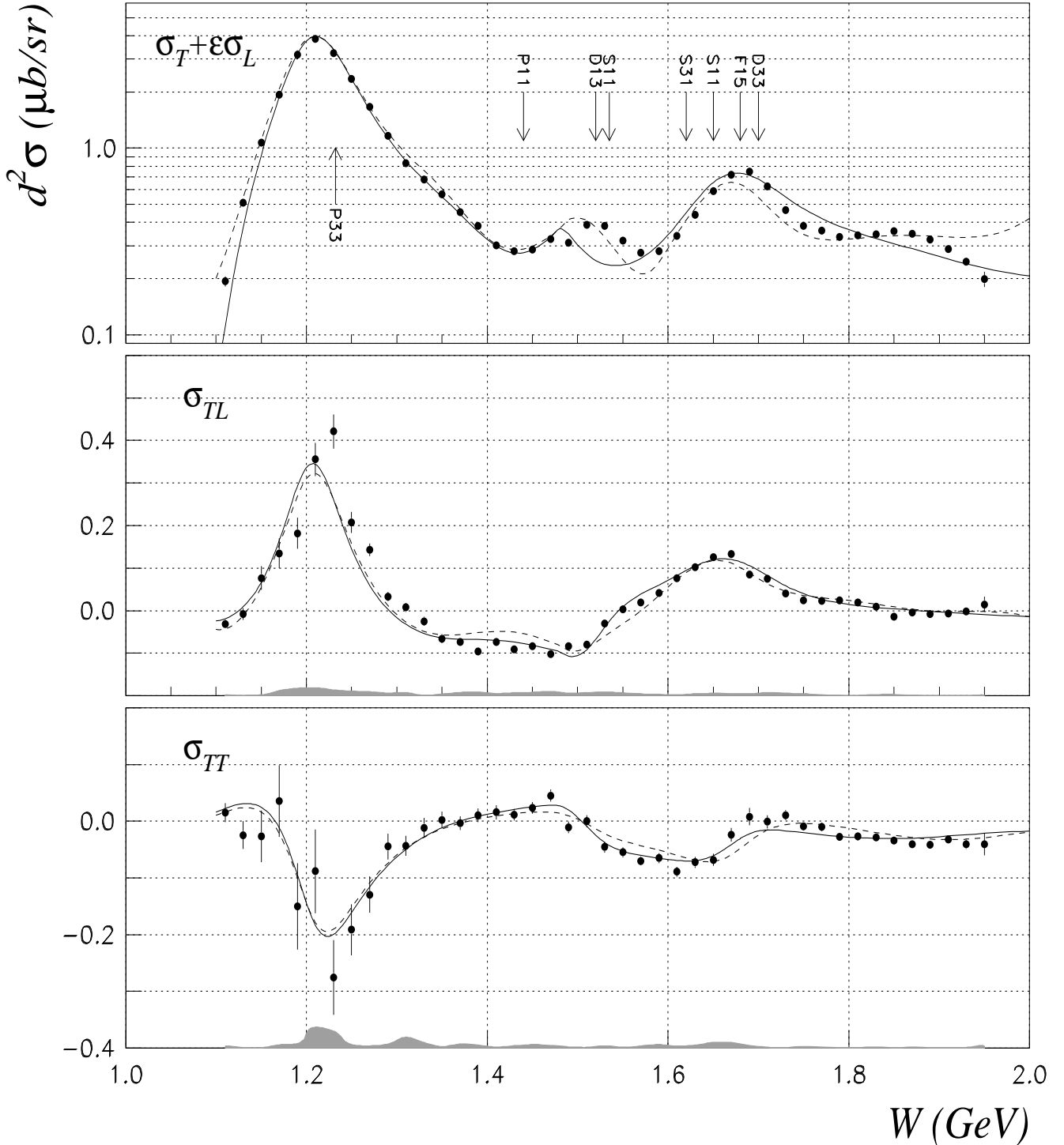


FIG. 10: Virtual photo-production cross sections for $\gamma^* p \rightarrow p\pi^0$ with statistical error bars as a function of W at $Q^2 = 1.0 \text{ GeV}^2$, $\cos \theta^* = -0.975$: $\sigma_T + \epsilon \sigma_L$, σ_{TL} and σ_{TT} . The one-sigma value of the total systematic errors is given for the σ_{TL} and σ_{TT} cross sections by the size of the shaded area at the bottom of each plot. The solid curves correspond to the MAID2003 *local fit*, and the dashed curves to SAID *WI03K solution* [6]. In the top part of the figure, we indicated the positions of the 8 most prominent resonances whose helicity amplitudes are adjusted in MAID2003 (see Section III B).

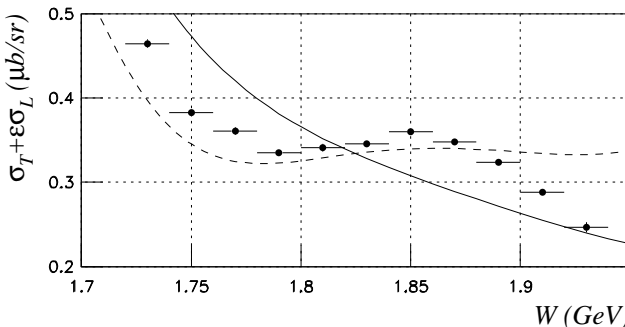


FIG. 11: The $\sigma_T + \epsilon \sigma_L$ cross section in a limited high W region at $Q^2 = 1.0 \text{ GeV}^2$, $\cos \theta^* = -0.975$. The full line corresponds to the MAID2003 *local fit* and the dashed line to the SAID *WI03K solution*.

Our results on b_{exp} yield new information on this topic especially for $W > 1.7 \text{ GeV}$ even if the contributions from resonant and non-resonant amplitudes are not separated.

A nontrivial W dependence of the parameter b_{exp} results from an interplay between contributions of the resonant and non-resonant amplitudes. The latter are known to be small around the $\Delta(1232)$ and increase monotonically with W . We find from the data that $b_{\text{exp}} \approx 0$ in the range of $1.3 < W < 1.4 \text{ GeV}$, which indicates a cancellation of the different Q^2 dependences of the resonant (especially P_{11} -Roper) and non-resonant amplitudes. The dominance of the resonant amplitude M_{1+} in the range $W < 1.3 \text{ GeV}$ results in $b_{\text{exp}} \approx 1 - 2 \text{ GeV}^{-2}$, and $b_{\text{exp}} \approx 1 - 1.5 \text{ GeV}^{-2}$ in the range $W > 1.6 \text{ GeV}$ where non-resonant terms start to dominate.

In summary, we have measured in the resonance region the three partial cross sections $\sigma_T + \epsilon \sigma_L$, σ_{TT} , and σ_{TL} for the reaction $\gamma^* p \rightarrow p\pi^0$ at $Q^2 = 1 \text{ GeV}^2$ and backward angles. We have obtained the Q^2 dependence for the cross section integrated over angle ϕ : $\int d\sigma d\phi = \sigma_T + \epsilon \sigma_L$. These data will be used to constrain models. A first step was done for the Unitary Isobar Model MAID2000 [1, 2]. From this analysis, we find new constraints on the R_{EM} and R_{SM} ratios of the $\Delta(1232)$ resonance (Table V). In spite of the agreement between our data and the calculation, the Q^2 dependence of the total cross section is not reproduced by MAID2000. On the other hand we observe a substantial improvement in the Q^2 dependence shown in Fig. 9 when our MAID2003 *local fit* is used.

The MAID and SAID analyses employ fundamentally different techniques for describing the scattering ampli-

tude. Our data result in significant readjustments in the parameters of both models, and throughout the entire W range. Although the results of the model calculations agreed initially very poorly with our data, a joint analysis with the world dataset resulted in a much improved description of the data. This is explained by evident limitations in the kinematics of the pre-existing dataset for even the relatively simple $\gamma^* p \rightarrow p\pi^0$ reaction, particularly at high W . For both MAID and SAID, our data show strong sensitivity to the $P_{11}(1440)$ Roper resonance, as evidenced by the large changes in the new fits to this region of the spectrum.

Finally, although our results are not sufficient to allow a full partial-wave analysis in the high W region (between 1.7 and 2.0 GeV), the position of the enhancement of $\sigma_T + \epsilon \sigma_L$ (see Fig. 11) is fully consistent with the recent analysis of Chen *et al.* [46]. The dynamical model used in [46] implies that the third S_{11} resonance should have a mass $1846 \pm 47 \text{ MeV}$. Evidences of missing resonances in this region have also been shown in pion electroproduction at CLAS [47], in kaon photoproduction at SAPHIR [48] and CLAS [49], and in $\pi N \rightarrow \pi\eta$ [50]. All these recent publications demonstrate the interest of both theoreticians and experimentalists in a detailed understanding of the nucleon resonance region, and point out the need for accurate data in meson electro- and photo-production.

The underlying physics of the nucleon resonances and the transition to deep inelastic scattering is still under investigation. Therefore, new data on exclusive processes as a function of both W and Q^2 are of great value.

Acknowledgments

We wish to acknowledge accelerator staff who delivered the beam, as well as the Hall A technical staff. We are grateful to the SAID group for useful discussions and for providing the updated fits. This work was supported by DOE contract DE-AC05-84ER40150 under which the Southeastern Universities Research Association (SUR) operates the Thomas Jefferson National Accelerator Facility. We acknowledge additional grants from the US DOE and NSF, the French Centre National de la Recherche Scientifique and Commissariat à l'Energie Atomique, the Conseil Régional d'Auvergne, the FWO-Flanders (Belgium) and the BOF-Gent University.

[1] D. Drechsel, O. Hanstein, S. S. Kamalov, and L. Tiator, Nucl. Phys. **A645**, 145 (1999), nucl-th/9807001, URL <http://www.kph.uni-mainz.de/MAID/>.

[2] S. S. Kamalov, D. Drechsel, O. Hanstein, L. Tiator, and S. N. Yang, Nucl. Phys. **A684**, 321 (2001).

[3] L. Tiator *et al.* (2003), nucl-th/0310041.

[4] R. A. Arndt, I. I. Strakovsky, and R. L. Workman, Phys. Rev. **C53**, 430 (1996), nucl-th/9509005.

[5] R. A. Arndt, W. J. Briscoe, I. I. Strakovsky, and R. L. Workman, Phys. Rev. **C66**, 055213 (2002), nucl-th/0205067.

[6] R. Arndt, W. Briscoe, I. Strakovsky, and R. Workman

(2003), nucl-th/0301068.

[7] P. Y. Bertin, C. Hyde-Wright, P. A. M. Guichon, et al. (1993), experiment E93-050, URL <http://hallaweb.jlab.org/experiment/E93-050/vcs.html>

[8] N. Isgur and G. Karl, Phys. Rev. **D19**, 2653 (1979).

[9] R. Koniuk and N. Isgur, Phys. Rev. Lett. **44**, 845 (1980).

[10] R. Koniuk and N. Isgur, Phys. Rev. **D21**, 1868 (1980).

[11] R. Koniuk, Nucl. Phys. **B195**, 452 (1982).

[12] S. Capstick and W. Roberts, Phys. Rev. **D49**, 4570 (1994), nucl-th/9310030.

[13] R. Bijker, F. Iachello, and A. Leviatan, Phys. Rev. **C54**, 1935 (1996), nucl-th/9510001.

[14] I. Niculescu et al., Phys. Rev. Lett. **85**, 1186 (2000).

[15] I. Niculescu et al., Phys. Rev. Lett. **85**, 1182 (2000).

[16] R. M. Davidson, N. C. Mukhopadhyay, and R. S. Wittman, Phys. Rev. **D43**, 71 (1991).

[17] I. G. Aznaurian, Phys. Rev. **D57**, 2727 (1998), hep-ph/9708238.

[18] I. G. Aznauryan, Phys. Rev. **C67**, 015209 (2003), nucl-th/0206033.

[19] D. Drechsel and L. Tiator, eds., *Workshop on the Physics of Excited Nucleons* (World Scientific, 2001).

[20] S. Dytman and E. Swanson, eds., *Workshop on the Physics of Excited Nucleons* (World Scientific, 2002).

[21] R. Siddle et al., Nucl. Phys. **B35**, 93 (1971).

[22] S. Galster et al., Phys. Rev. **D5**, 519 (1972).

[23] J. C. Alder et al., Nucl. Phys. **B46**, 573 (1972).

[24] J. C. Alder et al., Nucl. Phys. **B105**, 253 (1976).

[25] W. Albrecht et al., Nucl. Phys. **B25**, 1 (1970).

[26] W. Albrecht et al., Nucl. Phys. **B27**, 615 (1971).

[27] V. V. Frolov et al., Phys. Rev. Lett. **82**, 45 (1999), hep-ex/9808024.

[28] K. Joo et al. (CLAS), Phys. Rev. Lett. **88**, 122001 (2002), hep-ex/0110007.

[29] K. Joo et al. (CLAS), Phys. Rev. **C68**, 032201 (2003), nucl-ex/0301012.

[30] A. Biselli et al. (CLAS), Phys. Rev. **C68**, 035202 (2003), nucl-ex/0307004.

[31] J. Alcorn et al., accepted by NIM A.

[32] J. Denard, A. Saha, and G. Laveissiere (2001), presented at IEEE Particle Accelerator Conference (PAC2001), Chicago, Illinois, 18-22 Jun 2001.

[33] K. B. Unser, AIP Conf. Proc. **252**, 266 (1991).

[34] C. Hyde-Wright, L. Todor, and G. Laveissière, Tech. Rep. TN-01-001, JLab (2001).

[35] R. Suleiman, Tech. Rep. TN-98-007, JLab (1998).

[36] K. G. Fissum et al., Nucl. Instrum. Meth. **A474**, 108 (2001).

[37] *CEBAF Online Data Acquisition*, URL <http://coda.jlab.org>.

[38] E. A. J. M. Offerman et al., *ESPACE User's Guide* (1997), URL <http://hallaweb.jlab.org/espaces/docs.html>.

[39] S. Jaminion, Ph.D. thesis, Université Blaise Pascal (2001), DU 1259.

[40] L. Van Hoorebeke et al., to be submitted to NIM A.

[41] M. Vanderhaeghen, J. M. Friedrich, D. Lhuillier, D. Marchand, L. Van Hoorebeke, and J. Van de Wiele, Phys. Rev. **C62**, 025501 (2000), hep-ph/0001100.

[42] G. Laveissière, Ph.D. thesis, Université Blaise Pascal (2001), DU 1309.

[43] C. Jutier, Ph.D. thesis, Old Dominion University and Université Blaise Pascal (2001), DU 1298.

[44] Tables available at <http://hallaweb.jlab.org/experiment/E93-050/vcs.html>.

[45] G. Sterman and P. Stoler, Ann. Rev. Nucl. Part. Sci. **47**, 193 (1997), hep-ph/9708370.

[46] G.-Y. Chen, S. Kamalov, S. N. Yang, D. Drechsel, and L. Tiator, Nucl. Phys. **A723**, 447 (2003), nucl-th/0210013.

[47] M. Ripani et al. (2003), hep-ex/0304034.

[48] T. Mart and C. Bennhold, Phys. Rev. **C61**, 012201 (2000), nucl-th/9906096.

[49] J. W. C. McNabb et al. (The CLAS) (2003), nucl-ex/0305028.

[50] S. Capstick, T. S. H. Lee, W. Roberts, and A. Svarc, Phys. Rev. **C59**, 3002 (1999), nucl-th/9904005.

TABLE VI: $\sigma_T + \epsilon \sigma_L$ cross section at $Q^2 = 1.0 \text{ GeV}^2$ in $\mu\text{b} \cdot \text{sr}^{-1}$. The values are followed by the statistical and the total systematic errors.

W (MeV)	ϵ	$\cos \theta^* = -0.975$		$\cos \theta^* = -0.925$			$\cos \theta^* = -0.875$			$\cos \theta^* = -0.825$			
1110.0	0.945	0.194	± 0.012	± 0.006	0.241	± 0.018	± 0.008	0.300	± 0.028	± 0.010	0.313	± 0.045	± 0.010
1130.0	0.944	0.511	± 0.017	± 0.017	0.597	± 0.037	± 0.020	0.668	± 0.067	± 0.022	0.640	± 0.084	± 0.021
1150.0	0.942	1.068	± 0.034	± 0.035	0.965	± 0.086	± 0.032	0.933	± 0.105	± 0.031	0.996	± 0.116	± 0.034
1170.0	0.940	1.937	± 0.046	± 0.065	2.365	± 0.094	± 0.080	1.625	± 0.139	± 0.054	1.785	± 0.176	± 0.061
1190.0	0.938	3.176	± 0.049	± 0.108	3.591	± 0.102	± 0.124	3.518	± 0.167	± 0.118	3.074	± 0.186	± 0.101
1210.0	0.936	3.853	± 0.049	± 0.134	3.887	± 0.125	± 0.135	3.824	± 0.153	± 0.134	3.573	± 0.172	± 0.133
1230.0	0.934	3.221	± 0.048	± 0.109	3.171	± 0.130	± 0.105	3.385	± 0.153	± 0.115	3.687	± 0.175	± 0.125
1250.0	0.932	2.348	± 0.033	± 0.080	2.645	± 0.064	± 0.088	2.287	± 0.155	± 0.076	2.451	± 0.177	± 0.082
1270.0	0.930	1.665	± 0.021	± 0.056	1.832	± 0.039	± 0.061	1.828	± 0.110	± 0.060	1.602	± 0.181	± 0.054
1290.0	0.927	1.162	± 0.015	± 0.039	1.302	± 0.038	± 0.045	1.307	± 0.088	± 0.044	1.155	± 0.132	± 0.039
1310.0	0.925	0.832	± 0.012	± 0.029	0.893	± 0.042	± 0.037	0.912	± 0.078	± 0.041	0.973	± 0.123	± 0.042
1330.0	0.922	0.680	± 0.013	± 0.023	0.686	± 0.040	± 0.023	0.770	± 0.073	± 0.031	0.681	± 0.118	± 0.023
1350.0	0.920	0.566	± 0.012	± 0.019	0.641	± 0.034	± 0.021	0.643	± 0.078	± 0.022	0.611	± 0.138	± 0.027
1370.0	0.917	0.455	± 0.010	± 0.016	0.501	± 0.034	± 0.017	0.414	± 0.080	± 0.024	0.147	± 0.131	± 0.007
1390.0	0.914	0.385	± 0.010	± 0.013	0.375	± 0.036	± 0.021	0.387	± 0.086	± 0.032	0.128	± 0.161	± 0.008
1410.0	0.910	0.301	± 0.010	± 0.010	0.349	± 0.036	± 0.021	0.309	± 0.079	± 0.025	0.023	± 0.122	± 0.013
1430.0	0.907	0.281	± 0.008	± 0.011	0.344	± 0.031	± 0.016	0.441	± 0.102	± 0.018	0.160	± 0.151	± 0.009
1450.0	0.903	0.286	± 0.007	± 0.011	0.371	± 0.029	± 0.019	0.271	± 0.087	± 0.014	-0.002	± 0.171	± 0.009
1470.0	0.900	0.327	± 0.008	± 0.012	0.329	± 0.036	± 0.019	0.255	± 0.132	± 0.024			
1490.0	0.896	0.311	± 0.008	± 0.011	0.460	± 0.048	± 0.029	0.364	± 0.123	± 0.030			
1510.0	0.892	0.388	± 0.008	± 0.013	0.430	± 0.036	± 0.015	0.314	± 0.114	± 0.011			
1530.0	0.887	0.383	± 0.007	± 0.013	0.488	± 0.032	± 0.016	0.409	± 0.135	± 0.014			
1550.0	0.883	0.319	± 0.006	± 0.011	0.396	± 0.051	± 0.021	-0.111	± 0.168	± 0.013			
1570.0	0.878	0.276	± 0.005	± 0.009	0.461	± 0.059	± 0.032	-0.176	± 0.214	± 0.009			
1590.0	0.873	0.281	± 0.005	± 0.011	0.376	± 0.055	± 0.013	-0.107	± 0.142	± 0.019			
1610.0	0.868	0.339	± 0.005	± 0.013	0.428	± 0.040	± 0.018	-0.112	± 0.157	± 0.004			
1630.0	0.863	0.439	± 0.006	± 0.018	0.450	± 0.064	± 0.020						
1650.0	0.857	0.590	± 0.006	± 0.028	0.602	± 0.085	± 0.040						
1670.0	0.852	0.719	± 0.008	± 0.041	0.606	± 0.085	± 0.046						
1690.0	0.845	0.749	± 0.010	± 0.048	0.535	± 0.106	± 0.018						
1710.0	0.839	0.625	± 0.007	± 0.035	-0.069	± 0.187	± 0.003						
1730.0	0.832	0.465	± 0.005	± 0.024	0.348	± 0.063	± 0.022						
1750.0	0.826	0.383	± 0.004	± 0.016	0.281	± 0.042	± 0.015						
1770.0	0.818	0.361	± 0.005	± 0.013	0.082	± 0.079	± 0.007						
1790.0	0.811	0.335	± 0.004	± 0.011									
1810.0	0.803	0.341	± 0.005	± 0.011									
1830.0	0.795	0.346	± 0.004	± 0.011									
1850.0	0.786	0.360	± 0.004	± 0.012									
1870.0	0.777	0.348	± 0.004	± 0.011									
1890.0	0.768	0.323	± 0.004	± 0.011									
1910.0	0.759	0.288	± 0.004	± 0.010									
1930.0	0.749	0.247	± 0.006	± 0.008									
1950.0	0.738	0.199	± 0.019	± 0.007									

TABLE VII: σ_{TL} cross section at $Q^2 = 1.0 \text{ GeV}^2$ in $\mu\text{b} \cdot \text{sr}^{-1}$. The values are followed by the statistical and the total systematic errors.

W (MeV)	ϵ	$\cos \theta^* = -0.975$			$\cos \theta^* = -0.925$			$\cos \theta^* = -0.875$			$\cos \theta^* = -0.825$		
		-0.032	± 0.009	± 0.001	-0.087	± 0.015	± 0.003	-0.076	± 0.024	± 0.003	-0.079	± 0.038	± 0.003
1110.0	0.945	-0.032	± 0.009	± 0.001	-0.087	± 0.015	± 0.003	-0.076	± 0.024	± 0.003	-0.079	± 0.038	± 0.003
1130.0	0.944	-0.008	± 0.013	± 0.001	-0.039	± 0.032	± 0.002	-0.045	± 0.058	± 0.002	0.003	± 0.071	± 0.003
1150.0	0.942	0.077	± 0.028	± 0.003	0.216	± 0.074	± 0.007	0.413	± 0.089	± 0.014	0.400	± 0.097	± 0.014
1170.0	0.940	0.135	± 0.035	± 0.012	0.094	± 0.076	± 0.020	0.896	± 0.114	± 0.031	0.986	± 0.142	± 0.033
1190.0	0.938	0.182	± 0.037	± 0.018	0.418	± 0.087	± 0.033	0.879	± 0.137	± 0.033	1.529	± 0.148	± 0.051
1210.0	0.936	0.356	± 0.039	± 0.019	0.922	± 0.110	± 0.042	1.619	± 0.129	± 0.055	2.072	± 0.139	± 0.069
1230.0	0.934	0.421	± 0.040	± 0.014	1.141	± 0.111	± 0.040	1.537	± 0.128	± 0.054	1.796	± 0.141	± 0.062
1250.0	0.932	0.208	± 0.025	± 0.011	0.502	± 0.052	± 0.025	1.182	± 0.128	± 0.046	1.489	± 0.143	± 0.056
1270.0	0.930	0.143	± 0.015	± 0.010	0.293	± 0.033	± 0.016	0.601	± 0.091	± 0.025	1.112	± 0.146	± 0.049
1290.0	0.927	0.033	± 0.011	± 0.007	0.201	± 0.033	± 0.014	0.426	± 0.074	± 0.022	0.773	± 0.109	± 0.035
1310.0	0.925	0.008	± 0.010	± 0.008	0.129	± 0.037	± 0.031	0.359	± 0.061	± 0.038	0.467	± 0.092	± 0.042
1330.0	0.922	-0.025	± 0.011	± 0.001	0.067	± 0.035	± 0.009	0.146	± 0.059	± 0.031	0.392	± 0.085	± 0.027
1350.0	0.920	-0.066	± 0.010	± 0.004	-0.056	± 0.029	± 0.009	0.044	± 0.064	± 0.022	0.164	± 0.104	± 0.015
1370.0	0.917	-0.073	± 0.008	± 0.008	-0.067	± 0.027	± 0.011	0.094	± 0.066	± 0.027	0.387	± 0.104	± 0.019
1390.0	0.914	-0.096	± 0.008	± 0.008	-0.038	± 0.028	± 0.018	0.001	± 0.062	± 0.025	0.205	± 0.115	± 0.009
1410.0	0.910	-0.073	± 0.009	± 0.005	-0.088	± 0.029	± 0.021	-0.004	± 0.058	± 0.026	0.233	± 0.089	± 0.019
1430.0	0.907	-0.091	± 0.007	± 0.007	-0.110	± 0.026	± 0.017	-0.140	± 0.076	± 0.020	0.125	± 0.113	± 0.008
1450.0	0.903	-0.084	± 0.006	± 0.008	-0.155	± 0.024	± 0.020	-0.005	± 0.070	± 0.021	0.238	± 0.130	± 0.013
1470.0	0.900	-0.102	± 0.007	± 0.011	-0.101	± 0.026	± 0.016	-0.046	± 0.071	± 0.017			
1490.0	0.896	-0.084	± 0.007	± 0.006	-0.138	± 0.034	± 0.030	-0.032	± 0.076	± 0.031			
1510.0	0.892	-0.079	± 0.007	± 0.008	-0.056	± 0.029	± 0.018	0.083	± 0.078	± 0.019			
1530.0	0.887	-0.030	± 0.005	± 0.009	-0.017	± 0.026	± 0.020	0.092	± 0.092	± 0.022			
1550.0	0.883	0.003	± 0.005	± 0.007	0.030	± 0.030	± 0.029	0.277	± 0.092	± 0.023			
1570.0	0.878	0.019	± 0.004	± 0.005	0.047	± 0.036	± 0.036	0.266	± 0.097	± 0.029			
1590.0	0.873	0.041	± 0.005	± 0.003	0.098	± 0.037	± 0.022	0.180	± 0.104	± 0.021			
1610.0	0.868	0.076	± 0.005	± 0.003	0.127	± 0.029	± 0.006	0.390	± 0.105	± 0.015			
1630.0	0.863	0.102	± 0.005	± 0.005	0.157	± 0.036	± 0.007						
1650.0	0.857	0.125	± 0.005	± 0.006	0.217	± 0.046	± 0.024						
1670.0	0.852	0.133	± 0.007	± 0.005	0.339	± 0.050	± 0.026						
1690.0	0.845	0.085	± 0.009	± 0.005	0.198	± 0.051	± 0.008						
1710.0	0.839	0.075	± 0.006	± 0.008	0.092	± 0.054	± 0.005						
1730.0	0.832	0.041	± 0.004	± 0.006	0.117	± 0.037	± 0.017						
1750.0	0.826	0.025	± 0.004	± 0.005	0.031	± 0.025	± 0.011						
1770.0	0.818	0.023	± 0.004	± 0.003	0.064	± 0.047	± 0.015						
1790.0	0.811	0.024	± 0.004	± 0.001									
1810.0	0.803	0.020	± 0.004	± 0.001									
1830.0	0.795	0.010	± 0.004	± 0.003									
1850.0	0.786	-0.014	± 0.003	± 0.003									
1870.0	0.777	-0.004	± 0.004	± 0.001									
1890.0	0.768	-0.008	± 0.004	± 0.000									
1910.0	0.759	-0.006	± 0.004	± 0.000									
1930.0	0.749	-0.002	± 0.006	± 0.000									
1950.0	0.738	0.015	± 0.018	± 0.001									

TABLE VIII: σ_{TT} cross section at $Q^2 = 1.0 \text{ GeV}^2$ in $\mu b \cdot sr^{-1}$. The values are followed by the statistical and the total systematic errors.

W (MeV)	ϵ	$\cos \theta^* = -0.975$			$\cos \theta^* = -0.925$			$\cos \theta^* = -0.875$			$\cos \theta^* = -0.825$		
		0.015	± 0.016	± 0.001	0.039	± 0.021	± 0.002	0.044	± 0.034	± 0.002	0.002	± 0.048	± 0.001
1110.0	0.945	-0.024	± 0.025	± 0.001	-0.016	± 0.044	± 0.001	-0.071	± 0.068	± 0.002	-0.034	± 0.079	± 0.002
1130.0	0.944	-0.026	± 0.045	± 0.001	-0.269	± 0.086	± 0.009	-0.445	± 0.097	± 0.015	-0.437	± 0.105	± 0.015
1150.0	0.940	0.035	± 0.063	± 0.006	0.040	± 0.094	± 0.014	-0.845	± 0.124	± 0.028	-1.194	± 0.141	± 0.040
1170.0	0.938	-0.150	± 0.076	± 0.008	-0.358	± 0.127	± 0.014	-0.917	± 0.164	± 0.031	-1.825	± 0.177	± 0.064
1190.0	0.936	-0.088	± 0.074	± 0.037	-0.836	± 0.146	± 0.043	-1.644	± 0.170	± 0.063	-2.342	± 0.201	± 0.084
1210.0	0.934	-0.275	± 0.066	± 0.030	-1.152	± 0.135	± 0.079	-1.611	± 0.151	± 0.083	-1.897	± 0.184	± 0.086
1230.0	0.932	-0.191	± 0.045	± 0.007	-0.557	± 0.072	± 0.039	-1.117	± 0.133	± 0.061	-1.507	± 0.155	± 0.075
1250.0	0.930	-0.129	± 0.032	± 0.004	-0.391	± 0.054	± 0.022	-0.668	± 0.102	± 0.040	-1.283	± 0.143	± 0.050
1270.0	0.927	-0.045	± 0.023	± 0.007	-0.256	± 0.051	± 0.009	-0.643	± 0.093	± 0.025	-0.948	± 0.128	± 0.035
1290.0	0.925	-0.043	± 0.018	± 0.019	-0.174	± 0.050	± 0.007	-0.388	± 0.094	± 0.013	-0.598	± 0.142	± 0.020
1310.0	0.922	-0.011	± 0.017	± 0.010	-0.168	± 0.042	± 0.023	-0.267	± 0.075	± 0.012	-0.508	± 0.135	± 0.041
1330.0	0.920	0.002	± 0.015	± 0.003	-0.034	± 0.032	± 0.015	-0.109	± 0.068	± 0.012	-0.321	± 0.128	± 0.054
1350.0	0.917	-0.004	± 0.012	± 0.007	-0.003	± 0.033	± 0.001	-0.233	± 0.068	± 0.008	-0.516	± 0.116	± 0.027
1390.0	0.914	0.011	± 0.012	± 0.005	-0.070	± 0.037	± 0.021	-0.151	± 0.084	± 0.031	-0.537	± 0.164	± 0.019
1410.0	0.910	0.016	± 0.012	± 0.002	-0.004	± 0.034	± 0.019	-0.132	± 0.078	± 0.028	-0.516	± 0.123	± 0.025
1430.0	0.907	0.012	± 0.010	± 0.004	0.040	± 0.029	± 0.009	0.003	± 0.095	± 0.016	-0.258	± 0.139	± 0.010
1450.0	0.903	0.023	± 0.010	± 0.006	0.091	± 0.029	± 0.009	-0.114	± 0.080	± 0.006	-0.466	± 0.160	± 0.018
1470.0	0.900	0.045	± 0.011	± 0.005	0.013	± 0.043	± 0.015	-0.163	± 0.156	± 0.022			
1490.0	0.896	-0.011	± 0.010	± 0.002	0.069	± 0.055	± 0.028	-0.182	± 0.143	± 0.036			
1510.0	0.892	0.000	± 0.011	± 0.002	-0.057	± 0.042	± 0.005	-0.298	± 0.132	± 0.010			
1530.0	0.887	-0.045	± 0.010	± 0.004	-0.071	± 0.040	± 0.004	-0.221	± 0.156	± 0.008			
1550.0	0.883	-0.055	± 0.009	± 0.002	-0.196	± 0.067	± 0.016	-0.914	± 0.216	± 0.031			
1570.0	0.878	-0.070	± 0.008	± 0.004	-0.105	± 0.075	± 0.037	-0.883	± 0.282	± 0.030			
1590.0	0.873	-0.065	± 0.008	± 0.006	-0.210	± 0.072	± 0.011	-0.817	± 0.164	± 0.049			
1610.0	0.868	-0.089	± 0.009	± 0.004	-0.228	± 0.054	± 0.011	-0.756	± 0.206	± 0.025			
1630.0	0.863	-0.072	± 0.010	± 0.005	-0.375	± 0.091	± 0.012						
1650.0	0.857	-0.068	± 0.011	± 0.010	-0.225	± 0.114	± 0.017						
1670.0	0.852	-0.024	± 0.012	± 0.010	-0.271	± 0.120	± 0.011						
1690.0	0.845	0.008	± 0.015	± 0.005	-0.182	± 0.147	± 0.050						
1710.0	0.839	-0.001	± 0.011	± 0.002	-0.829	± 0.260	± 0.050						
1730.0	0.832	0.011	± 0.009	± 0.001	0.012	± 0.097	± 0.000						
1750.0	0.826	-0.009	± 0.007	± 0.003	0.030	± 0.063	± 0.002						
1770.0	0.818	-0.010	± 0.007	± 0.002	-0.318	± 0.124	± 0.024						
1790.0	0.811	-0.027	± 0.006	± 0.001									
1810.0	0.803	-0.026	± 0.007	± 0.001									
1830.0	0.795	-0.028	± 0.006	± 0.002									
1850.0	0.786	-0.034	± 0.007	± 0.001									
1870.0	0.777	-0.041	± 0.007	± 0.002									
1890.0	0.768	-0.041	± 0.007	± 0.001									
1910.0	0.759	-0.033	± 0.007	± 0.001									
1930.0	0.749	-0.041	± 0.008	± 0.002									
1950.0	0.738	-0.041	± 0.019	± 0.002									